Magnetic anisotropy in CoNi nanowire arrays: Analytical calculations and experiments

L. G. Vivas,[1,*] M. Vazquez,[1] J. Escrig,[2] S. Allende,[2] D. Altbir,[2] D. C. Leitao,[3,4] and J. P. Araujo[4]

[1]*Institute of Materials Science of Madrid, CSIC, 28049 Madrid, Spain*

[2]*Departamento de Física, Universidad de Santiago de Chile (USACH) and Center for the Development of Nanoscience and Nanotechnology (CEDENNA), Avenida Ecuador 3493, 9170124 Santiago, Chile*

[3]*INESC-MN and IN, Institute of Nanoscience and Nanotechnology, Rua Alves Redol 9, 1000-029 Lisboa, Portugal*

[4]*IFIMUP and IN, Institute of Nanoscience and Nanotechnology, Department of Physics and Astronomy, Faculdade de Cências da Universidade do Porto, Rua do Campo Alegre, 678, 4169-007, Porto, Portugal*

(Received 10 August 2011; revised manuscript received 5 October 2011; published 24 January 2012)

Ordered arrays of Co_xNi_{1-x} nanowires ($0 < x < 1$) were fabricated by a template-assisted method using electrodeposition into anodic aluminum oxide membranes. Tuning of the Co-alloy composition by changing the Ni content enables control of the effective anisotropy axis, which is determined by the balance between the hcp and fcc magnetocrystalline and shape anisotropies. We report on the nanowires' structural and magnetic properties (e.g., hysteresis curves and their parameters as well as first-order reversal curve analysis), paying particular attention to their angular dependence. It is confirmed that the crystal phase of nanowires with length 2.5 μm and diameter 35 nm shifts from hcp to fcc as the Ni content increases. That results in a significant modification of the magnetization process and, accordingly, of the magnetic properties of the array. Analytical calculations of the angular dependence of the coercivity allow us to confirm that the magnetization reversal is mostly ascribed to the propagation of a transverse domain wall. Fitting of the experiment to these calculations indicates the presence of a transverse crystalline anisotropy (ascribed to the hcp phase) in Co wires, while this changes to an axial anisotropy (fcc phase) as the Ni content increases.

DOI: 10.1103/PhysRevB.85.035439 PACS number(s): 75.10.−b, 75.60.−d, 75.60.Jk

I. INTRODUCTION

During recent years, a great effort toward further development of highly ordered arrays of nanostructures has been carried out due to their technological applications in a wide range of areas such as semiconductors, optics, and biomedical and data storage devices.[1–4] Different lithographic techniques can be used to grow magnetic nanowires (NWs); nevertheless they are usually very expensive and time consuming. Alternatively, researchers have turned their efforts to straightforward chemical template-based methods combined with high-yield electrochemical deposition techniques. A widespread example is anodic aluminum oxide (AAO) membranes, which stand as a quite versatile and nearly inexpensive bottom-up technique to fabricate, at nanoscale, arrays with reproducible properties. The main advantage of AAO membranes resides in the ability to customize geometrical features, such as nanopore diameter, length, and periodicity, by simply changing the anodization conditions. Hence, several studies concerning single-element magnetic NW arrays of Ni, Co, Fe, and their alloys can be found in the literature.[5–8] Their magnetic behavior encloses both the magnetic character of individual NWs as well as the strength of the interwire magnetostatic interactions. The latter is a function of the geometric characteristics of the template, mainly its periodicity. For many purposes, e.g., perpendicular magnetic recording, a well-defined out-of-plane effective magnetic anisotropy is desired, which denotes the existence of a magnetization easy axis parallel to the NW direction. However, while the strong shape anisotropy of the NWs favors such magnetic alignment, interwire magnetostatic interactions result in a reduction of the effective longitudinal anisotropy. This effect translates into a decrease of the coercive field and remanence of the array.[9,10] The magnetization reversal mode of NW arrays with diameter in the range of tens of nanometers has been investigated in previous work.[11–16] Three main idealized modes of the magnetization reversal process have been identified: coherent rotation (C) with all the spins rotating simultaneously; the transverse wall (T) in which spins reverse progressively via propagation of a transverse domain wall; and the vortex wall (V) in which spins reverse progressively via propagation of a vortex (curling) domain wall. The applicability of any mode depends on the geometrical characteristics. Since coercivity is directly related to the reversal mechanism, one alternative is to induce different reversal modes by modifying external parameters, such as the direction of the applied field. On the other hand, analyses of the magnetization process by measuring first-order reversal curves[17] (FORCs) have been proved to be powerful in gaining further insight into the relevance of the contributions of reversible and irreversible mechanisms. Electrodeposited Co NWs usually show a preferential hexagonal close-packed (hcp) crystallographic structure, with the c axis nearly perpendicular to the NW axis.[18] The presence of such a hcp phase gives rise to a significant magnetocrystalline anisotropy contribution that competes with the intrinsic shape anisotropy, which results in a decrease of the effective uniaxial anisotropy of the system.[19] The properties of electroplated Co can be tailored by changing the electroplating time (and consequently the length[20] of the NWs), pH,[21] plating current,[22] or temperature,[23] thus enabling the formation of a fcc phase and reinforcing the uniaxial anisotropy.[24] On the other hand, the magnetic properties of Co NWs can also be tuned by modifying the composition. For example, the addition of Ni allows one to partly retain the large saturation magnetization and high coercivity of Co, while enhancing the uniaxial anisotropy. Therefore, appropriate addition of Ni can be a simple and controllable route to tune the magnetic properties of Co NWs. In this work we establish

a correlation between structural properties of CoNi NWs with their magnetic anisotropy and the magnetization reversal mode. From the angular dependence of the coercivity, and considering the corresponding magnetocrystalline anisotropy term, we have inferred that the actual magnetization reversal mode occurs by propagation of a transverse wall. In addition, the FORC analysis indicates the presence of intense dipolar magnetic fields for Co NWs when compared to the CoNi ones. We attribute this effect again to the increase of the axial anisotropy on the addition of Ni.

A. Background on reversal processes in NWs

The study of reversal modes in elongated NWs is a classical micromagnetism problem.[25,26] For cylinders with diameters in the range of tens to hundreds of nanometers, coherent and curling reversal modes are considered. Nevertheless, when the wires are long enough, other modes can be energetically more favorable. Recent analytical calculations by some of the present authors[27] have led to determination of the angular dependence of the reversal modes, which led us to obtain the coercive field (H_c^k) for each of the reversal mechanisms $k = C$, T, and V.

The classical angular dependence of the nucleation for coherent magnetization reversal was calculated by Stoner and Wohlfarth[28] and is given by

$$H_n^C(\theta) = -\frac{2[K_{sh}(L_{nw}) + K_{mc}]\sqrt{1 - t^2 + t^4}}{\mu_0 M_0^2(1 + t^2)} M_0, \quad (1)$$

where $t = \tan(\theta)^{1/3}$ with θ being the angle between the long axis of the wire and the applied field; M_0 is the saturation magnetization and L_{nw} is the length of the wire. In addition, $K_{sh}(L_{nw}) = \frac{1}{4}\mu_0 M_0^2[1 - 3N_z(L_{nw})]$ is the shape anisotropy constant and K_{mc} denotes the magnetocrystalline anisotropy constant. The demagnetizing factor of a wire along the z axis, $N_z(L_{nw})$, has been previously obtained.[29]

Recently, Landeros *et al.*[30] calculated the total energy for the transverse reversal mode, considering the sum of exchange and dipolar contributions. Then they minimized the energy with regard to the domain wall width (ω_T). The nucleation or coercive field was calculated by Escrig *et al.*,[12,27] assuming that for magnetization reversal by means of the nucleation and propagation of a transverse wall the field is equal to the nucleation field of an equivalent system with an effective volume that reverses its magnetization by coherent rotation. Then, the Stoner-Wohlfarth model can be adapted[27,31] to describe the angular dependence of the transverse reversal mode by replacing the length of the whole structure by the reduced length of the involved domain wall with width ω_T:

$$H_n^T(\theta) = -\frac{2[K_{sh}(\omega_T) + K_{mc}]\sqrt{1 - t^2 + t^4}}{\mu_0 M_0^2(1 + t^2)} M_0, \quad (2)$$

where $K_{sh}(\omega_T) = \frac{1}{4}\mu_0 M_0^2[1 - 3N_z(\omega_T)]$ is the shape anisotropy constant. It is important to mention that the expressions for $H_n^T(\theta)$ and $H_n^C(\theta)$ differ only in the length. In coherent reversal, L_{nw} represents the total length of the wire, and thus the coercivity varies with the length. However, in the transverse mode, and because the field is nearly independent of the length of the wire, as shown by Landeros *et al.*,[30] the coercivity is also independent of the length. Then, for long enough wires ($L_{nw} > \omega_T$), the transverse mode will always exhibit a lower coercivity, irrespective of θ. As shown in the Stoner-Wohlfarth model, the coercivity for coherent and transverse reversal modes can be written as a function of the nucleation field as

$$H_c^{C(T)}(\theta) = \begin{cases} \left|H_n^{C(T)}(\theta)\right|, & 0 \leqslant \theta \leqslant \pi/4, \\ 2\left|H_n^{C(T)}(\pi/4)\right| - \left|H_n^{C(T)}(\theta)\right|, & \pi/4 \leqslant \theta \leqslant \pi/2. \end{cases} \quad (3)$$

Thus, in very short wires ($L_{nw} \approx \omega_T$) the high energy cost involved in the creation of a domain wall is responsible for the coherent rotational magnetization reversal.

The angular dependence of the curling nucleation field in a prolate spheroid was calculated first by Aharoni[32] in 1997. The effect of adding a magnetic anisotropy is essentially the same as that of changing the shape anisotropy by changing the aspect ratio. The effect is far from being negligible, and the anisotropy must be taken into account. Thus we obtain the following expressions for the nucleation field:

$$H_n^V(\theta)\cos(\theta - \gamma) = \{N_x(L_{nw})\sin^2(\gamma) + N_z(L_{nw})\cos^2(\gamma) - c - d[3\cos^2(\gamma) - 1]\}M_0, \quad (4)$$

$$H_n^V(\theta)\sin(\theta - \gamma) = \left[[(N_x(L_{nw}) - N_z(L_{nw}) + d]\left(\frac{\sin(2\gamma)}{2}\right)\right]M_0, \quad (5)$$

where $c = \frac{q^2 L_{ex}^2}{R^2}$, $d = \frac{K_{mc}}{\mu_0 M_0^2}$, $L_{ex} = \sqrt{2A/\mu_0 M_0^2}$ is the exchange length, R is the radius of the wire, and γ is the angle at which the nucleation starts, measured from the wire axis. For a cylindrical geometry, Shtrikman and Treves[33] obtained $q^2 = 1.08\pi$. To obtain the nucleation field $H_n^V(\theta)$, we simultaneously solve numerically Eqs. (4) and (5) for each applied field angle. As pointed out by Aharoni,[32] a jump of the magnetization for an isolated system occurs at or near the vortex nucleation field. Therefore, the coercivity is quite close to the absolute value of the nucleation field, and we assume here, as in other studies,[34] that in the V mode $-H_n^V$ is a good approximation to the coercivity H_c^V.

II. EXPERIMENTAL DETAILS

Highly ordered AAO membranes were prepared by a two-step anodization process of a high-purity Al foil.[35] After electropolishing,[36] the anodization was performed in a 0.3M oxalic acid solution at 2 °C temperature under an applied potential of 40 V. The first anodization step was performed for 24 h, while the second step lasted for 1 h. The AAO obtained is then characterized by the presence of an array of self-ordered nanopores with a diameter ($D = 2R$) of about 35 nm, arranged in a dense hexagonal lattice with a periodicity of ∼105 nm. The length of the nanopores (or that of the final wires, L_{nw}) depends on the duration of the second anodization step, and is set to $L_{nw} = 2.5$ μm. The AAO is then used as a template for the growth of the metallic NWs by electrodeposition. However, the presence of an insulating alumina barrier layer

at the bottom of each nanopore prevents a direct deposition of material. Therefore, a suitable chemical process is used to reduce the thickness of the barrier layer, resulting in the formation of dendrites, thus enabling the subsequent filling of pores with metals by a pulsed-electrodeposition method.[5]

The dendrites were filled with Au,[37] and then the cylindrical main pores were filled with Co, $Co_{80}Ni_{20}$, $Co_{50}Ni_{50}$, or Ni NWs. Details regarding the electroplating conditions for these materials can be found elsewhere.[8,18] Morphological and structural characterizations of the samples were performed using a Philips XL3O scanning electron microscopy (SEM) and a X'Pert PRO x-ray diffractometer (XRD), respectively. All magnetic measurements were performed in a KLA-Tencor EV7 commercial vibrating-sample magnetometer. Measurements were done at room temperature as a function of the angle between the applied field and the NWs under a maximum applied field of 17 kOe.

III. RESULTS AND DISCUSSION

Figure 1 shows a SEM cross-sectional image of the AAO membrane and the embedded parallel nanowires. Their distinct contrast enables one to distinguish between the Au present at the very bottom (brighter) and the $Co_{50}Ni_{50}$ alloy on top (darker). Fluctuations in the length of the Au layer in the NWs are visible and they are further transmitted to the Co and Co-alloy NWs grown on top. The origin of such distinct sizes is attributed to the nonuniform barrier layer thickness. These fluctuations (less than 100 nm) are relatively small so that an average NW length close to the nominal length of the pores (2.5 μm) in the AAO can still be considered with an expected negligible influence on the magnetic properties. Figure 2 display the XRD θ-2θ scans corresponding to the Co, $Co_{80}Ni_{20}$, and $Co_{50}Ni_{50}$ NW arrays, from top to bottom. For the Co NW sample, only the (100) hcp-phase peak is detected at $2\theta = 41.7^\circ$, indicating a textured structure [Fig. 2(a)]. Although the presence of mixed fcc-hcp phases in electrodeposited Co NWs has been reported previously,[18] we did not observe the peak around 44.2° corresponding to the fcc (111) crystallographic phase.

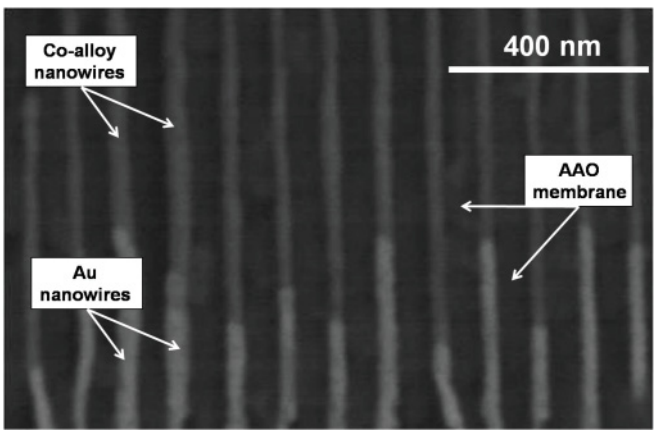

FIG. 1. Cross-sectional SEM image of $Co_{50}Ni_{50}$ NWs embedded in the AAO template. Dendrite structures shown at the bottom of the array are filled with Au (only the connection part of the dendrites to the main cylindrical NW is shown).

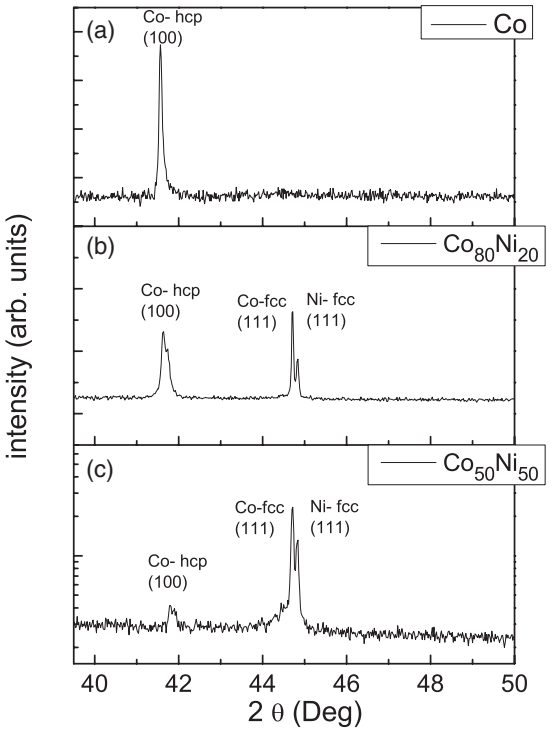

FIG. 2. XRD θ-2θ diffraction patterns of (a) Co, (b) $Co_{80}Ni_{20}$, and (c) $Co_{50}Ni_{50}$ NWs.

With the addition of Ni the size of the hcp (100) Co peak decreases significantly. Instead, two peaks are observed around 44.5°; they are more intense for $Co_{50}Ni_{50}$ (indicating a textured structure) than for $Co_{80}Ni_{20}$. At $2\theta = 44.2^\circ$ and 44.5° one expects the (111) Co fcc peak and the (111) Ni fcc peaks, respectively. This behavior indicates that the crystal structure of the nanowires has evolved from a hcp to a fcc phase.

A. Magnetization reversal and angular dependence of coercivity

Hysteresis loop measurements were performed under an external applied magnetic field parallel (∥) and perpendicular (⊥) to the NW axis, respectively. Figure 3 shows the room-temperature loops of the samples. Table I collects the main magnetic parameters, such as coercivity (H_c) and reduced remanence ($m_r = M_r/M_s$, where M_r is the remanent magnetization). From a comparative analysis, a weak effective longitudinal magnetic anisotropy can be assumed for Co NWs, since both $H_c^{\parallel}$ and $m_r^{\parallel}$ take slightly larger values than the corresponding perpendicular ones, reflecting competing magnetic anisotropies. While the textured (100) hcp phase of Co leads to a magnetocrystalline anisotropy with a perpendicular magnetic easy axis, one should note that the polycrystalline nature of the Co NWs should reduce the effective crystalline anisotropy. The latter, together with the strong shape anisotropy,[38] results in a preferential orientation of the magnetization parallel to the NWs. These observations are in agreement with previously reported data on polycrystalline Co NWs.[39,40] With the addition of Ni, a reinforcement of the parallel magnetic easy axis is observed, reflected in the increase of $H_c^{\parallel}$ and $m_r^{\parallel}$ and consequent decrease in $m_r^{\perp}$. However, an overall increase in

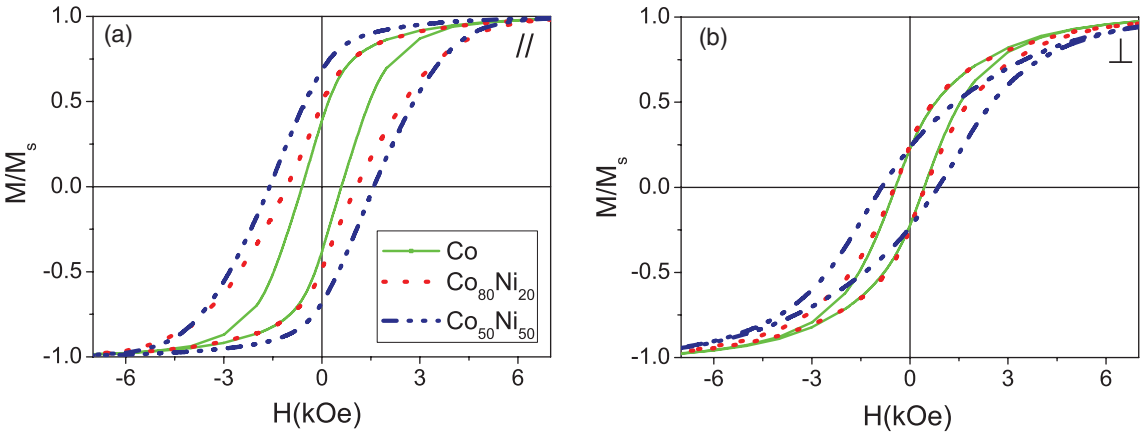

FIG. 3. (Color online) Reduced magnetization (M/M_s) hysteresis loops of Co, $Co_{80}Ni_{20}$, and $Co_{50}Ni_{50}$ NWs for (a) parallel and (b) perpendicular applied magnetic field.

$H_c^{\perp}$ is also visible. In this case, the polycrystallinity of the samples,[41] and the presence of both hcp and fcc phases, may lead to local crystal inhomogeneities, causing the observed increased irreversibility in the perpendicular $M(H)$ loop.

For the nanowires of 35 nm diameter presented here, the coercivity varies strongly (between 580 and 1590 Oe) and nonmonotonically as a function of the Ni content (see Table I). These results are in the same range as those obtained previously by Qin *et al.*;[42] however, those authors found that the coercivity decreases almost linearly with increasing Ni content. Nevertheless, those results correspond to different geometrical parameters as compared with the ones presented in this paper.

In order to analyze in further detail the actual magnetization reversal processes, the full angular dependence of hysteresis loops was measured. In particular, the experimental angular dependence of the coercivity can be compared with the expected evolution according to Eqs. (1) to (4), assuming the three possible reversal modes, i.e., coherent rotation and the nucleation and propagation of transverse and vortex domain walls. Figure 4(a) illustrates the results for Co NWs. Although all three modes are in principle possible, the system will reverse its magnetization by whichever mode opens an energetically accessible route first, that is, by the mode that offers the lowest coercivity. To obtain a good agreement with experiments, we considered for the calculations a magnetocrystalline anisotropy with an out-of-plane anisotropy constant of -8.62×10^4 J/m^3, which corresponds to a perpendicular easy plane. In this case we conclude that, independent of the angle, the magnetization reversal is driven by the nucleation and propagation of a transverse wall.

Figure 4(c) shows the results for the $Co_{50}Ni_{50}$ sample where similar calculations were performed. In this case, a better agreement with experiments is obtained by using a longitudinal anisotropy constant of 4.89×10^3 J/m^3, reflecting an axial easy axis. Again, the magnetization reverses by means of a transverse wall, although for angles around 60° the curling and the transverse reversal modes showed a very similar coercivity. In this case, thermal instability or shape irregularities, which are not considered in our model, can cause the system to adopt a vortex reversal mode. Similar studies were performed for $Co_{80}Ni_{20}$ and Ni NWs [See Figs. 4(b) and 4(d)]. Regarding the lack of perfect fitting for angles close to 0° and 90°, it is important to note that our model does not consider interelement interactions with surrounding wires. These interactions are responsible for an additional antiferromagnetic or ferromagnetic contribution to the field for 0° and 90°, respectively. Figure 5 collects the values of the crystalline anisotropy K_{mc} used in our calculations to obtain the best agreement with experimental results. From this figure we observe that the easy axis evolves from perpendicular (in the plane of the membrane) in the case of Co NWs to longitudinal (parallel to the wire axes) in the case of Ni-rich alloy NWs.

The effect of crystalline anisotropy on a particular magnetic element is to modify its fundamental magnetic properties, like its coercivity and remanence. In a certain range of magnetocrystalline anisotropy defining the second-easiest anisotropy axis for CoNi nanowires, the energy of the curling and the transverse reversal modes might be comparable. In this

TABLE I. Experimental magnetic parameters of Co, $Co_{80}Ni_{20}$, $Co_{50}Ni_{50}$, and Ni NW arrays extracted from major hysteresis curves and FORC diagrams (see text for the definitions of H_c, m_r, and $\langle H_c^F \rangle$.)

Sample	$H_c^{\parallel}$ (Oe)	$m_r^{\parallel}$	$H_c^{\perp}$ (Oe)	$m_r^{\perp}$	$\langle H_c^{F\parallel} \rangle$ (Oe)	$\langle H_c^{F\perp} \rangle$ (Oe)
Co	620	0.38	420	0.23	1130	600
$Co_{80}Ni_{20}$	1070	0.51	470	0.24	1540	820
$Co_{50}Ni_{50}$	1590	0.73	865	0.22	1800	1500
Ni	580	0.71	230	0.19		

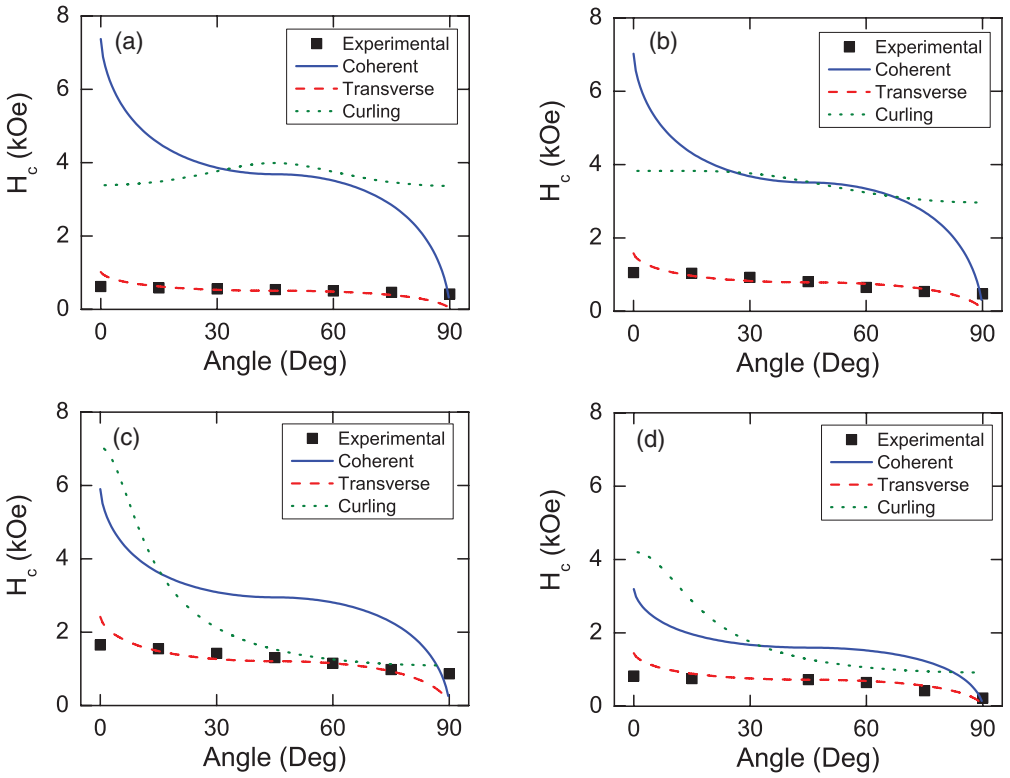

FIG. 4. (Color online) Experimental and calculated (according to the different modes) angular dependence of parallel coercivity for (a) Co, (b) $Co_{80}Ni_{20}$, (c) $Co_{50}Ni_{50}$, and (d) Ni NWs.

case the dynamical transitions between those modes might be observable during the magnetization reversal. The fits of Fig. 4, however, demonstrate that the transverse domain wall propagation possesses much lower coercivity than that of the curling process for the identical anisotropy value. Therefore the curling mode can be safely excluded from consideration.

B. FORC analysis

In order to obtain further insight into the magnetic properties of the systems, we obtained the FORC diagrams from a set of minor hysteresis loops. While major $M(H)$ hysteresis loops (MHLs) provide information regarding the global (average) behavior of the magnetic system, FORC measurements are more appropriate to investigate the processes taking place during the magnetization reversal. In particular, FORC measurements proved to be valuable in addressing the role of the distinct crystallographic contributions present in NWs,[38] being therefore complementary to the magnetic and structural characterizations presented.

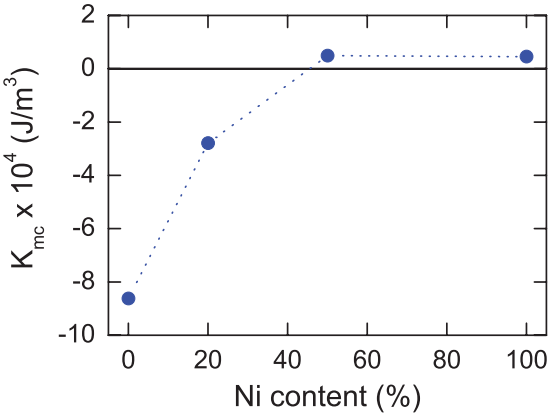

FIG. 5. (Color online) Fitted magnetocrystalline anisotropy constant K_{mc} as a function of Ni concentration.

For each minor loop, one starts from the magnetically saturated state; then the applied magnetic field is ramped down to a particular value, called the reversal field (H_r). Afterward, the magnetic field is increased back again toward the saturation value. This last part corresponds to the FORC and holds information from the previous minor loop. The FORC distribution (ρ) is thus obtained from a mixed second derivative of $M(H)$, given by[17]

$$\rho(H,H_r) = -\frac{1}{2}\frac{\partial^2 M(H,H_r)}{\partial H \partial H_r} \quad \text{for } H > H_r. \tag{6}$$

In this work, we performed a set of 100 FORC cycles, covering the region between the closure points of the hysteresis diagrams (field ranging from −5 to 5 kOe). The magnetic field was applied parallel and perpendicular to the NW longitudinal axis, and a reversal field step (ΔH_r) of 100 Oe was used. Figure 6 shows the parallel and perpendicular FORC diagrams for Co and $Co_{50}Ni_{50}$ NW arrays. Each diagram consists of a contour plot with a color scale from blue (minimum) to red (maximum).[39] In this representation, the H_u axis corresponds to the interaction field and H_{cr} denotes the coercive field, which may not correspond directly to the H_c obtained from the MHLs.[43] From the FORC diagram, one can obtain the

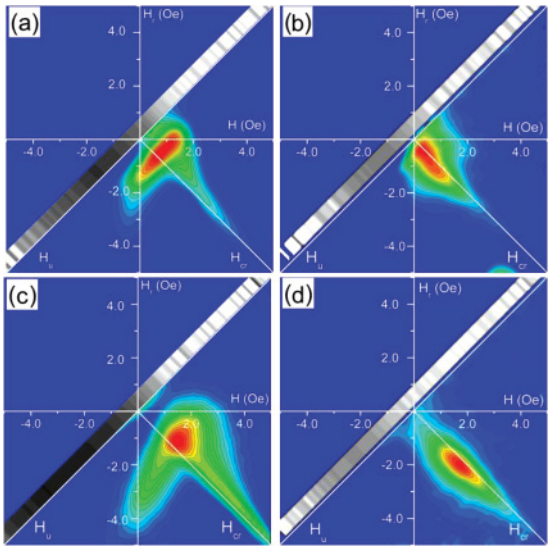

FIG. 6. (Color online) FORC diagrams for (a),(b) Co and (c),(d) $Co_{50}Ni_{50}$ NWs, obtained with the applied magnetic field parallel (a),(c) and perpendicular (b),(d) to the NW axis. The color scale goes from blue (representing the minimum) toward red (maximum values). The gray-scale strip in the diagrams denotes the reversibility indicator which ranges from white to black, corresponding to fully reversible and irreversible behavior, respectively.

coercivity $\langle H_c^F \rangle$ as the H_c position of the FORC distribution maximum. A detailed description regarding this representation and the physical analysis model used here can be found elsewhere.[43–47] For clarity, H_u and H_{cr} are defined as follows:

$$H_u = \frac{H + H_r}{2}, \quad H_{cr} = \frac{H - H_r}{2}. \tag{7}$$

In addition, the characterization of the reversible processes can be done through the calculation of a reversibility indicator (gray-scale strip in the diagrams), ranging from white to black, corresponding to fully reversible or irreversible behavior, respectively.[48] This indicator is obtained from the slope (χ_F) of the minor loops at each H_r, and reflects the reversibility of the process, normalized to the susceptibility (χ_{hyst}) of the MHL upper branch at the same H_r:

$$\eta(H = H_r) = \frac{\chi_F(H = H_r)}{\chi_{\text{hyst}}(H = H_r)}. \tag{8}$$

Figures 6(a) and 6(b) show respectively the parallel and perpendicular FORC diagrams for Co NWs. The parallel FORC diagram in Fig. 6(a) exhibits two distinct distributions. The main one, along the H_u axis, can be ascribed to the magnetostatic interactions among NWs. Each nanowire in the array interacts with the stray fields produced by the neighboring wires and experiences an antiferromagnetic-like coupling,[38,47] which acts as a macroscopic demagnetizing field.[35,44] In this regard, the effect of the magnetostatic interactions is equivalent to that of a perpendicular (in-plane) magnetic anisotropy. Thus, both the perpendicular magnetocrystalline anisotropy [(100) hcp Co phase] and magnetostatic interactions become stronger compared to the geometrical shape anisotropy. Enhanced dipolar interactions are also expected in pure Co nanowires as a consequence of a high saturation magnetization M_s. The second distribution (in the parallel Co FORC), observed along the H_{cr} axis, should be associated with a harder magnetization reversal process. As discussed by Pirota *et al.*,[46] the broadening of this distribution can be ascribed to the existence of a fcc phase, which requires a higher field to reverse the magnetization leading to the visible extended branch over H_{cr}. Notice that a clear maximum at $H_c^F(\text{fcc}) \approx 3.8$ kOe for a 20% (volume) fcc contribution in 1.7-μm-long Co NWs has been reported.[45] In our case, the absence of a maximum in this second distribution confirms a rather small contribution from fcc crystallites (lower than 10%).

In turn, the perpendicular FORC diagram in Fig. 6(b) shows less complex structure. A single main coercivity distribution is observed along the H_{cr} axis, which is attributed to the change of the main crystallographic hcp phase shown in the visible broadening of ρ originated by the NWs' polycrystalline nature, as concluded from XRD data (Fig. 2).

For $Co_{50}Ni_{50}$, the parallel and perpendicular FORC diagrams are shown in Figs. 6(c) and 6(d), respectively. For the parallel FORC diagram, two distributions are again observed, exhibiting a wider spread over both H_u and H_{cr} axes in comparison with those of Co nanowires. In this case, the presence of Co still favors the magnetostatic interactions among NWs, which is reflected in the elongation along H_u. However, with increasing Ni content the fcc phase is suggested to increase, shown by the presence of a broader distribution along the H_{cr} axis. Accordingly, the defined maximum of the coercivity distribution is shifted to higher fields in comparison with that in Co NWs. In addition, the maximum of ρ over H_{cr} is also detected at higher field (around 2.9 kOe), which can be attributed to the irreversible magnetization reversal of the fcc grains (lying parallel to the applied magnetic field).[48] Such a large irreversible contribution strongly favors magnetization reversal by nucleation and propagation of a transverse domain wall, as inferred from micromagnetic calculations. In contrast, the perpendicular FORC diagram [Fig. 6(d)] shows mainly a broad distribution along H_{cr}, which supports the transition from hcp to fcc phase, suggesting that the NWs may present a mixture of both fcc and hcp structures.

The average parallel, $\langle H_c^{F\parallel} \rangle$, and perpendicular, $\langle H_c^{F\perp} \rangle$, coercive fields derived from our FORC measurements are collected in Table I. Overall, an $\langle H_c^{F\parallel} \rangle$ increase is observed with increasing Ni content. This effect supports our previous assumptions derived from XRD and MHL measurements, indicating that the addition of fcc Ni leads to an increase in the fcc:hcp ratio, favoring the magnetic easy axis parallel to the NWs.

Finally, the reversibility indicator for parallel FORC diagrams denotes clearly a wider distribution of irreversible (dark gray) processes for $Co_{50}Ni_{50}$ NWs, attributed to the reduced contribution of hcp crystallites and correspondingly reduced perpendicular anisotropy, as discussed above. Regarding the perpendicular FORC diagrams, stronger irreversibilities are observed at low field for Co NWs. However, for $Co_{50}Ni_{50}$ NWs, the irreversibility distribution extends over a wider spectrum at higher fields, probably associated with the observed higher coercivity in MHL measurements.

IV. CONCLUSIONS

In conclusion, we have shown that the magnetic properties of electrodeposited Co and CoNi alloy NW arrays are strongly dependent upon the crystalline structure, which depends on the relative Ni content. The presence of a Co hcp phase leads to an important competition between shape and magnetocrystalline anisotropies, which translates into a weakly defined magnetization easy axis along the NW longitudinal direction. On the other hand, with increasing Ni content the net crystalline anisotropy drastically decreases and shape anisotropy becomes dominant. The angular dependence of coercivity has been modeled considering the different possible reversal modes. The propagation of a transversal wall gives the best fitting with experimental observations for all the NW alloy compositions. In addition, fitted values of the crystalline anisotropy confirm the evolution from perpendicular (in-plane) to parallel (out-of-plane) orientation of the magnetization easy axis. It is important to note that the magnetization reversal mode obtained is not intrinsic to Co or CoNi NWs but to a given shape (geometry) and crystalline anisotropy. Finally, FORC analysis gave us additional information on the role of each crystallographic phase present in the NWs, evidencing the presence of a hcp-fcc mixture in all samples. Moreover, the appearance of an irreversible magnetization reversal promoted by the presence of a higher proportion of fcc phase as the Ni content increases strongly correlates with our analytical calculations of the H_c angular dependence.

ACKNOWLEDGMENTS

This work was supported by the Spanish Ministry of Science and Innovation, MICINN (Project No. MAT2010-20798-C05-01), by the Chilean FONDECYT (Projects No. 1080300 and No. 1110784), and the Ministerio de Economía, Fomento y Turismo (Projects No. P10-061-F and FB0807). L.G.V. thanks International Iberian Nanotechnology Laboratory (INL) for financial support. D.C.L. acknowledges FCT Grant No. SFRH/BPD/72359/2010. J.P.A. thanks Fundação Gulbenkian for financial support within the "Programa Gulbenkian de Estímulo a Investigação Científica."

*lauragv@icmm.csic.es

[1] P. Yang, R. Yan, and M. Fardy, Nano Lett. **10**, 1529 (2010).
[2] Y. Nakayama, P. J. Pauzauskiel, A. R. Radenovic, R. M. Onorato, R. J. Saykally, J. Liphardt, and P. Yang, Nature (London) **447**, 1098 (2007).
[3] G. Zheng, F. Patolsky, Y. Cuil, W. U. Wang, and C. M. Lieber, Nat. Biotechnol. **23**, 1294 (2005).
[4] S.-M. Ahn, K.-W. Moon, C.-G. Cho, and S.-B. Choe, Nanotechnology **22**, 085201 (2011).
[5] M. Vazquez, M. Hernandez-Velez, A. Asenjo, D. Navas, V. M. Prida, K. Pirota, O. Sanchez, and J. L. Baldonedo, Physica B **384**, 36 (2006).
[6] X. Y. Zhang, L. H. Xu, J. Y. Dai, and H. L. W. Chan, Physica B **353**, 187 (2004).
[7] D. J. Sellmyer, M. Zheng, and R. Skomski, J. Phys.: Condens. Matter **13**, R433 (2001).
[8] D. C. Leitao, C. T. Sousa, J. Ventura, K. R. Pirota, M. Vazquez, J. B. Sousa, and J. P. Araujo, J. Magn. Magn. Mater. **322**, 1319 (2010).
[9] F. Zighem, T. Maurer, F. Ott, and G. Chaboussant, J. Appl. Phys. **109**, 013910 (2011).
[10] J. Escrig, D. Altbir, M. Jaafar, D. Navas, A. Asenjo, and M. Vazquez, Phys. Rev. B **75**, 184429 (2007).
[11] L. Sun, Y. Hao, C.-L. Chien, and P. C. Searson, IBM J. Res. Dev. **49**, 79 (2005).
[12] J. Escrig, R. Lavin, J. L. Palma, J. C. Denardin, D. Altbir, A. Cortes, and H. Gomez, Nanotechnology **19**, 075713 (2008).
[13] C. Tannous, A. Ghaddar, and J. Gieraltowski, Europhys. Lett. **91**, 17001 (2010).
[14] R. Wieser, U. Nowak, and K. D. Usadel, Phys. Rev. B **69**, 064401 (2004).
[15] R. Hertel and J. Kirschner, Physica B **343**, 206 (2004).
[16] H. Forster, T. Schrefl, D. Suess, W. Scholz, V. Tsiantos, R. Dittrich, and J. Fidler, J. Appl. Phys. **91**, 6914 (2002).
[17] I. D Mayergoyz, J. Appl. Phys. **57**, 3803 (1985).
[18] K. R. Pirota, and M. Vazquez, Adv. Eng. Mater. **7**, 1111 (2005).
[19] J. Sanchez-Barriga, M. Lucas, F. Radu, E. Martin, M. Multigner, P. Marin, A. Hernando, and G. Rivero, Phys. Rev. B **80**, 184424 (2009).
[20] L. G. Vivas, R. Yanes, O. Chubykalo-Fesenko, and M. Vazquez, Appl. Phys. Lett. **98**, 232507 (2011).
[21] V. R. Caffarena, A. P. Guimaraes, W. S. D. Folly, E. M. Silva, and J. L. Capitaneo, Mater. Chem. Phys. **107**, 297 (2008).
[22] M. Darques, A. Encinas, L. Vila, and L. Piraux, J. Phys.: Condens. Matter **16**, S2279 (2004).
[23] X. Han, Q. Liu, J. Wang, S. Li, Y. Ren, R. Liu, and F. Li, J. Phys. D **42**, 095005 (2009).
[24] M. Vazquez, and L. G. Vivas, Phys. Status Solidi B **248**, 2368 (2011).
[25] W. F. Brown, *Micromagnetics* (Krieger, New York, 1978).
[26] A. Aharoni, *Introduction to the Theory of Ferromagnetism* (Oxford University Press, Oxford, 1996).
[27] J. Escrig, J. Bachmann, J. Jing, M. Daub, D. Altbir, and K. Nielsch, Phys. Rev. B **77**, 214421 (2008).
[28] E. C. Stoner and E. P. Wohlfarth, Philos. Trans. R. Soc., A **240**, 599 (1948).
[29] I. Beleggia, S. Tandon, Y. Zhu, and M. De Graef, J. Magn. Magn. Mater. **272**, e1197 (2004).
[30] P. Landeros, S. Allende, J. Escrig, R. Salcedo, D. Altbir, and E. Vogel, Appl. Phys. Lett. **90**, 102501 (2007).
[31] R. Lavin, J. C. Denardin, J. Escrig, D. Altbir, A. Cortes, and H. Gomez, J. Appl. Phys. **106**, 103903 (2009).
[32] A. Aharoni, J. Appl. Phys. **82**, 1281 (1997).
[33] S. Shtrikman, and D. Treves, in *Magnetism*, edited by G. T. Rado and H. Suhl (Academic, New York, 1963), Vol. 3.
[34] Y. Ishii, J. Appl. Phys. **70**, 3765 (1991).
[35] K. Nielsch, R. B. Wehrspohn, J. Barthel, J. Kirschner, U. Gosele, S. F. Fischer, and H. Kronmuller, Appl. Phys. Lett. **79**, 1360 (2001).

[36]D. C. Leitao, A. Apolinario, C. T. Sousa, J. Ventura, J. B. Sousa, M. Vazquez, and J. P. Araujo, J. Phys. Chem. C **115**, 8567 (2011).
[37]Z. Wang and M. Brust., Nanoscale Res. Lett. **2**, 34 (2007).
[38]R. Ferre, K. Ounadjela, J. M. George, L. Piraux, and S. Dubois, Phys. Rev. B **56**, 14066 (1997).
[39]H. Schlorb, V. Haehnel, M. S. Khatri, A. Srivastav, A. Kumar, L. Schultz, and S. Fahler, Phys. Status Solidi B **247**, 2364 (2010).
[40]A. Ghahremaninezhad and A. Dolati, J. Alloys Compd. **480**, 275 (2009).
[41]S. Thongmee, H. L. Pang, J. B. Yi, J. Ding, J. Y. Lin, and L. H. Van, Acta Mater. **57**, 2482 (2009).
[42]D. H. Qin, C. W. Wang, Q. Y. Sun, and H. L. Li, Appl. Phys. A **74**, 761 (2002).
[43]F. Beron, L. Clime, M. Ciureanu, D. Menard, R. W. Cochrane, and A. Yelon, J. Appl. Phys. **101**, 09J107 (2007).
[44]C. R. Pike, Phys. Rev. B **68**, 104424 (2003).
[45]M. Ciureanu, F. Beron, P. Ciureanu, R. W. Cochrane, D. Menard, A. Sklyuyev, and A. Yelon, J. Nanosci. Nanotechnol. **8**, 5725 (2008).
[46]K. R. Pirota, F. Beron, D. Zanchet, T. C. R. Rocha, D. Navas, J. Torrejon, M. Vazquez, and M. Knobel, J. Appl. Phys. **109**, 083919 (2011).
[47]F. Beron, D. Menard, and A. Yelon, J. Appl. Phys. **103**, 07D908 (2008).
[48]F. Beron, L.-P. Carignan, D. Menard, and A. Yelon, in *Electrodeposited Nanowires and Their Applications*, edited by N. Lupu (InTech, 2010), p. 167.